Springer

Acta Mechanica Sinica

CrossMark click for updates

• RESEARCH PAPER •

Acta Mech. Sin., Vol. 39, 323061 (2023)
https://doi.org/10.1007/s10409-023-23061-x

Wake of a bio-inspired flapping wing with morphing wingspan

Xinyi He[1], Yi Liu[1], Yixin Chen[1,2], and Shizhao Wang[1,2*]

[1] *The State Key Laboratory of Nonlinear Mechanics, Institute of Mechanics, Chinese Academy of Sciences, Beijing 100190, China;*
[2] *School of Engineering Sciences, University of Chinese Academy of Sciences, Beijing 101408, China*

Received March 29, 2023; accepted April 6, 2023; published online June 6, 2023

This work uses a bio-inspired flapping wing model to numerically investigate the effect of morphing wingspan on wake structures. The model consists of a rectangular flat-plate wing heaving harmonically in a uniform incoming flow at the Reynolds number of 300 and Strouhal number of 0.3. The wingspan changes during heaving, with a maximum wingspan at the middle of downstroke and minimum wingspan at the middle of upstroke. The wake is characterized by two oblique chains of interconnected vortex loops. Although the morphing wingspan has little effect on the wake topology, it significantly affects the magnitude and size of the vortices near the wing surface, which leads to an asymmetric distribution of vortex loop chains in the wake. The shrinking of leading-edge vortex under the lower surface of the wing in downstroke and the destructive interaction of tip vortices in upstroke are identified as the two vortex dynamics corresponding to the asymmetric wake structures. The analysis on the lift coefficients shows that the above vortex interactions are mainly caused by the change of span length instead of spanwise velocity.

Morphing wingspan, Wake structures, Flapping wing, Leading-edge vortex, Tip votices

Citation: X. He, Y. Liu, Y. Chen, and S. Wang, Wake of a bio-inspired flapping wing with morphing wingspan, Acta Mech. Sin. **39**, 323061 (2023), https://doi.org/10.1007/s10409-023-23061-x

1. Introduction

Wake has been widely investigated in biolocomotion [1-8] and has provided a feasible way to understand the complex vortex dynamics in swimming and flying. Natural swimmers and flyers have wings or fins with complex kinematics and geometric shapes. Simplified flapping wing models are usually used to clarify the interactions between fluids and wings/fins. The flapping foils in three-dimensional (2D) flows have successfully modeled the large aspect-ratio flapping wings or fins, and helped to identify the typical vortex phenomena in biolocomotion, such as the generation of leading-edge vortex [9-13], formation of reverse Karmann vortex street [14-19], interaction of wake vortices [20-24], and transition of wake patterns [25-30].

The wake of flapping foils in 2D flows consists of infinite long vortex tubes because of the ignorance of spanwise variation. The flapping low-aspect-ratio wing improved the 2D flapping foil by taking into account the effect of finite wingspan, resulting in a wake consisting of vortex loops. von Ellenrieder et al. [31] visualized the wake structures of a flapping rectangular wing with an aspect ratio of 3 by flow dyeing. The wing heaves and pitches in a uniform incoming flow at a Reynolds number of 164. By varying the Strouhal number (based on the flapping frequency and tip-to-tip amplitude) from 0.2 to 0.4, they show that the wake is featured by a chain of zigzag connected vortex loops. Blondeaux et al. [32] found that the dynamics of vortex loop depends on the Strouhal number and the wake pattern might change at relatively high Strouhal number. Dong et al. [33] numerically investigated the wake of flapping thin ellipsoid wings with three finite different aspect ratios ranging from 1.27 to 5.09. The flow structures are investigated in detail for the case with a Reynolds number of 200 and Strouhal number of 0.6. The wakes are found to be dominated by two chains of interconnected vortex loops that convect downstream at

*Corresponding author. E-mail address: wangsz@lnm.imech.ac.cn (Shizhao Wang)
Executive Editor: Guowei He

an angle with respect to the wake centerline. Buchholz and Smits [34, 35] identified three types of wake patterns by visualizing the vortex structures of a pitching rectangular flat plate wing at different Strouhal numbers. The three types of wake patterns are: (1) a zigzag chain of interconnected vortex loops when the Strouhal number is approximately between 0.2 and 025, (2) two oblique chains of interconnected vortex loops when the Strouhal number is approximately between 0.25 and 0.5, (3) wake of type II but with additional vortex structures forms from the streamwise vortex when the Strouhal number is higher than 0.5. These three types of wake patterns are confirmed by the consequent works [36-40]. The wake structures are found to be quite robust within a certain Strouhal number range, and not sensitive to the changes of wing planform, kinematics, and the Reynolds number.

The above studies established a general wake pattern paradigm for flapping low-aspect-ratio wing. However, most of the studies use a flapping wing model with a fixed wingspan. An important characteristic of three-dimensional flapping wing motion, the wingspan morphing, has not been included in those models. The morphing wingspan widely exists in the flight of birds and bats [41-45]. Birds and bats often extend their wings during downstroke, and retract their wings during upstroke. The ratio between the minimum and maximum wingspan in a slow-flying bat can be as low as 0.6 [45]. Hedenström et al. [46] showed that the bat flight generates a more complex wake consisting of multiple-connected vortex loops. Wang et al. [47] simulated a flapping rectangular flat plate with morphing wingspan, and found that the morphing wingspan can significantly affect the evolution of leading-edge vortex. But the effects of morphing wingspan on wake have not been reported in details. The relation between the morphing wingspan and the generation of the more complex wake is still not clear.

This work aims to look into the effect of morphing wingspan on the wake generated by flapping wings. The vortices in the wake are investigated by numerically simulating the flows around a bio-inspired flapping wing model, which isolates the spanwise morphing from the complex morphology and flapping kinematics of real flyers. The details of the generation and evolution of vortices in the wake are reported and compared with those generated by flapping wings with fixed wingspan. The effects of morphing wingspan on lift coefficients are also investigated. The organization of the paper is as follows. The numerical model and method are reported in Sect. 2. The characteristics and evolution of wake structures are reported in Sect. 3. The relations among the morphing wingspan, vortex structures and lift coefficient are discussed in Sect. 4. Finally, conclusions are drawn in Sect. 5.

2. Numerical model and method

2.1 Numerical model

This work uses the same bio-inspired morphing wing model as that in Wang et al. [47]. For the completeness, the model is briefly described as follows. The model wing has a flat-plate cross section with zero thickness and a chord length, and heaves vertically in an incoming uniform flow, U_∞, as shown in Fig. 1. The heaving is specified as

$$z_c = z_0 + A\sin(2\pi f t), \tag{1}$$

where z_c is the vertical position of the flapping wing center, z_0 is the time-averaged vertical position of the flapping wing center, A and f are flapping amplitude and frequency, respectively, and t is time. All the variables in Eq. (1) are non-dimensional. The characteristic length, velocity, time, and fluid density are the chord length c, the upstream flow velocity U_∞ , the reference time c/U_∞, and the fluid density ρ, respectively. The flapping Strouhal number is defined as $St = 2A^* f^*/U_\infty$, where A^* and f^* are the dimensional flapping amplitude and frequency, respectively. For convenience, a non-dimensional time $T = t - 0.25$ is used to describe the kinematics of the wing, according to which the downstroke of the wing starts at $T = 0, 1, 2, ...$, and so on.

The wingspan varies with time during the flapping. The length of the wingspan is specified as

$$L(t) = L_0[a - b\sin(2\pi f t + \varphi)], \tag{2}$$

where L_0 is the maximum wingspan, a and b (with the constraint of $a + b = 1$) are the parameters to control the ratio between the maximum and minimum wingspan, and φ is the phase difference between the heaving motion and the spanwise motion. The morphing wingspan results in a dynamically changing aspect ratio of

$$AR(t) = L(t)/c. \tag{3}$$

An example of the phase relation between heaving and spanwise morphing is illustrated in Fig. 2, for the case of

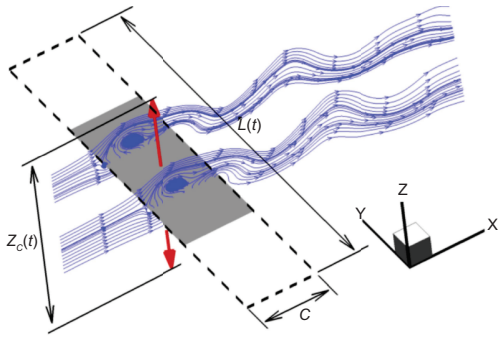

Figure 1 Schematic of flapping rectangular wing with morphing wingspan.

$\varphi = \pi/2$, $a = 0.75$, $b = 0.25$.

The flow around the flapping wing is determined by the incompressible Navier-Stokes equations and the mass conservation constraint:

$$\frac{\partial \mathbf{u}}{\partial t} + \mathbf{u} \cdot \nabla \mathbf{u} = -\nabla p + \frac{1}{Re}\nabla^2 \mathbf{u} + \mathbf{f}, \tag{4}$$

$$\nabla \cdot \mathbf{u} = 0, \tag{5}$$

where $\mathbf{u}$ and p are the non-dimensional velocity and pressure, $\mathbf{f}$ is a body force to represent the effect of boundaries on the flow in immersed boundary (IB) method, and $Re = U_\infty c/\nu$ is the Reynolds number, where ν is the kinematic viscosity of fluid. The non-dimensional vorticity is calculated by $\omega = \nabla \times \mathbf{u}$.

2.2 Numerical method and settings

Equations (4) and (5) are solved numerically by using an IB method based on the discrete stream-function formulation [48]. In this method, the flow field is solved on the Eulerian grid by using the discrete stream-function method (or the null space method, the exact projection method), in which the mass conservation constraint is satisfied in the level of machine precision. The body force that represents the effect of boundary on the flow is calculated implicitly by solving a linear equation to ensure the non-slip boundary condition, in which a discrete delta function provided by Yang et al. [49] is used. The computational scheme has formally second-order accuracy in time and space. The details of the numerical method can be found in the previous work [48].

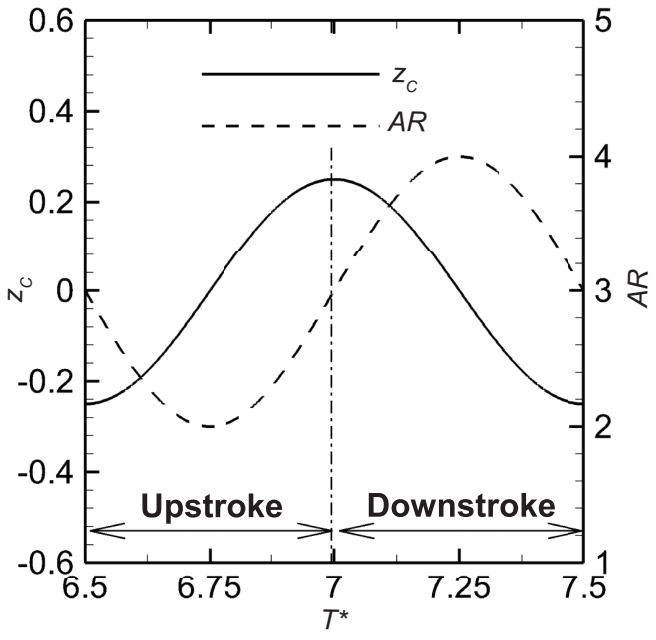

Figure 2 Histories of the heaving and spanwise morphing.

According to the robustness of the lift and flow structures reported in Wang et al. [48] where they varied flapping amplitude, flapping frequency, maximum aspect-ratio, phase lag between the heaving and spanwise motion, and span ratio (the ratio between the minimum wingspan and maximum wingspan), this work uses a typical case to investigate the evolution of the wake structures. The flapping and morphing parameters of this typical case are as follows: the flapping Strouhal number $St = 0.3$, the flapping amplitude $A = 0.25$, the phase difference between the spanwise motion and heaving $\varphi = \pi/2$, the span ratio $SR = L_{\min}/L_{\max} = 0.5$, the maximum aspect ratio $AR = L_{\max}/c = 4$, the time-averaged vertical position of the center of the wing $z_0 = 0$, and the geometric angle of attack of the wing $\alpha = 0$. The wingspan varies from 2 to 4 in this case. We refer to this typical case as the "morphing wingspan case" hereafter. Two additional cases with the same heaving kinematics but with the fixed wingspan are also investigated to help to identify the effect of morphing wingspan on wake structures. These two fixed wingspan cases have the parameters as follows: (1) $St = 0.3$, $A = 0.5$, $\varphi = \pi/2$, $SR = L_{\min}/L_{\max} = 1.0$, $AR = L_{\max}/c = 4$, $z_0 = 0$, and (hereafter refer to as the fixed wingspan case with) (2) $St = 0.3$, $A = 0.25$, $\varphi = \pi/2$, $SR = L_{\min}/L_{\max} = 1.0$, $AR = L_{\max}/c = 2$, $z_0 = 0$, and $\alpha = 0$ (hereafter refer to as the fixed wingspan case with $AR = 2$). Notice that the span ratio $SR = L_{\min}/L_{\max} = 1.0$ means that the wingspan remains fixed during the flapping. The Reynolds number is fixed at 300 in this study, considering that the wake structures are not sensitive to the Reynolds number for a flapping wing with sharp leading-edge [33, 34].

The computational domain is $[-16, 32] \times [-16, 16] \times [-24, 24]$ in the streamwise, spanwise and vertical directions, respectively. The uniform streamwise velocity is set at the inlet, and the free convection boundary condition is set at the outlet. The non-slip boundary condition is imposed at the surface of flapping wing. The zero-shear slip wall is used on the other boundaries. The computational domain size has been tested to assure that it is sufficiently large for development of the wake structures. The unstructured Cartesian grid with hanging node is used to refine the Eulerian grid around the wing and in the wake. The minimum Eulerian grid length $dh = 0.02$ is used in a region of $[-1, 1] \times [-3, 3] \times [-1, 1]$ around the flapping wing, and the grid length $dh = 0.04$ is used in a region of $[-2, 16] \times [-4, 4] \times [-6, 6]$ to resolve the flow structures in the wake. The time step is calculated dynamically by fixing the maximum Courant-Friedrichs-Lewy (CFL) number at 0.5. The distance among the Lagrangian grids varies as the wingspan changes during the flapping. The Lagrangian grid length is set as $0.01 \leq ds \leq 0.02$. The validations of the numerical method can be found in our previous work [48, 50, 51]. The test of grid-size independences was

conducted in a fixed wingspan case with $AR = 2$. The results showed the lift coefficient with the minimum Eulerian grid length of $dh = 0.02$ matched perfectly with that on a finer mesh with the minimum Eulerian grid length of $dh = 0.01$.

3. Wake

We use the λ_2 criterion introduced by Jeong and Hussain [52] to identify the vortex structures near wing and behind wings. Figure 3 plots the vortex structures around the wings of the morphing and fixed wingspans. In both cases, the wake structures behind the wings consist of two oblique chains of interconnected vortex loops. Therefore, the morphing wingspan does not change the wake pattern. However, the morphing wingspan significantly changes the vortex structures near wings, leading to an asymmetric distribution of vortex loops in the vertical direction. It is also noted that the vortex intensities become smaller with AR decreasing.

In the rest part of this section, the wake structures behind the fixed wingspan will be discussed in Sect. 3.1, which is used as a baseline to investigate the effect of morphing wingspan on wake structures. The wake structures behind the morphing wingspan are studied in Sect. 3.2 and used to understand the effect of morphing wingspan on wake.

3.1 Wake pattern for fixed wingspans

It is observed from Fig. 3(b) and (c) that two vortex loops with the opposite signs in each flapping period are generated by flapping of the wing with the fixed wingspans. The two vortex loops have the same geometry and vorticity magnitude. They shed in the consecutive flapping periods and connect to each other. Two oblique chains are formed by vortex loops and move downstream in a 'V' shape with a separation in the vertical direction.

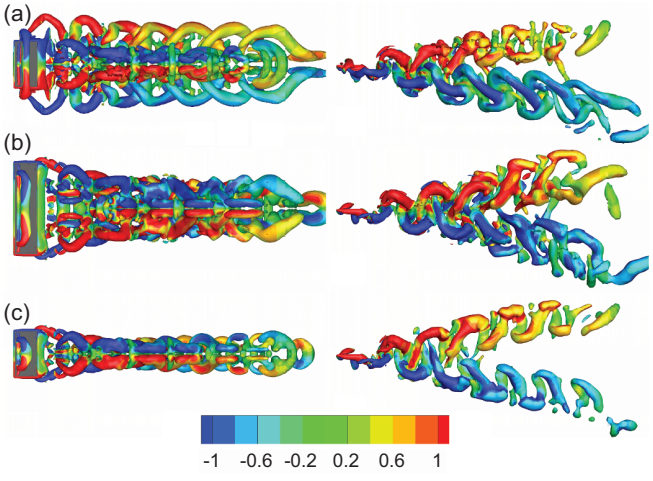

Figure 3 The top-view (left column) and side-view (right column) of vortex structures in the flapping rectangular when the wing is at the middle upstroke, (a) the morphing wingspan case, (b) the fixed wingspan case with $AR = 4$, (c) the fixed wingspan case with $AR = 2$. The iso-surfaces of $\lambda_2 = -0.1$ are shown. The gray (color online) indicates the value of non-dimensional streamwise vorticity ω_x.

Figure 4 plots the vortex loops for the flapping wings with the morphing and fixed wingspan at the end of downstroke. The vortex loops in the wakes are generated by leading-edge, trailing-edge and wing-tips, such as the leading-edge vortex V3 and the tip vortices TV2 in Fig. 4(b). The sizes of the vortex loops in Fig. 4(a) are comparable with those in Fig. 4(b) but larger than those in Fig. 4(c).

Figure 5 plots the vortex loops for the flapping wings with the morphing and fixed wingspan at the middle of upstroke. In Fig. 5(b), the tip vortices TV2 are convected downward during the upstroke and are connected to V4 near trailing-edge. The vortices V2, TV2 and V4 are connected to form a vortex loop which moves downward and is convected

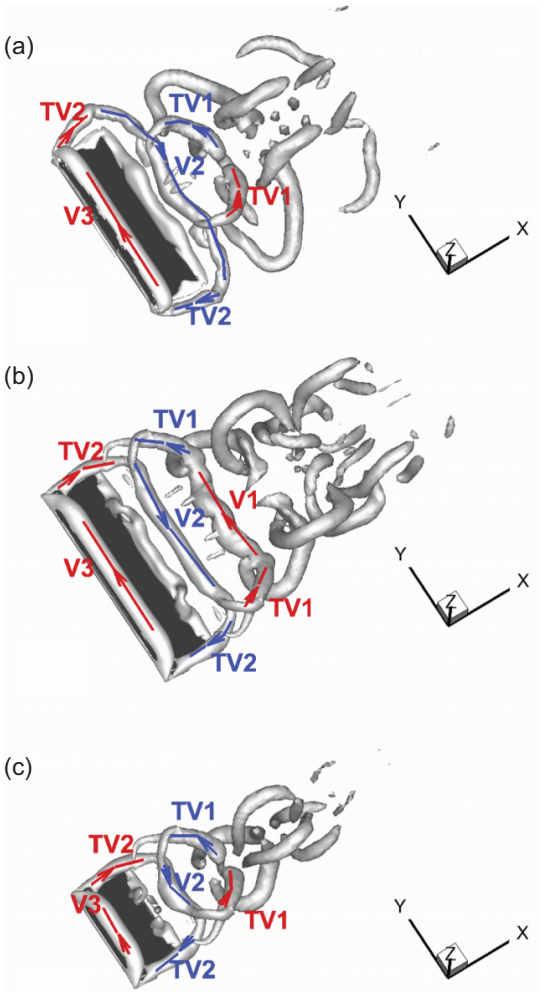

Figure 4 Vortex structures of the flapping rectangular wing at the instant when the wing is at the end of downstroke, (a) the morphing wingspan case, (b) the fixed wingspan case with $AR = 4$, (c) the fixed wingspan case with $AR = 2$. The flow structures are identified by the iso-surfaces of $\lambda_2 = -4$.

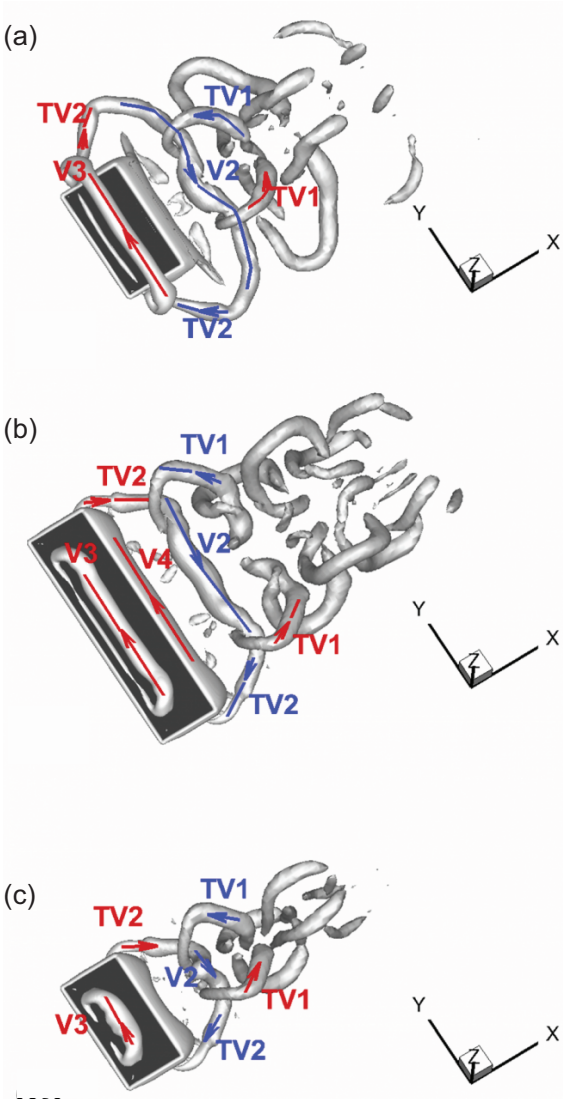

Figure 5 Vortex structures of the flapping rectangular wing at the instant when the wing is at the middle upstroke, (a) the morphing wingspan case, (b) the fixed wingspan case with $AR = 4$, (c) the fixed wingspan case with $AR = 2$. The flow structures are identified by the iso-surface of $\lambda_2 = -4$.

downstream. In comparison with Fig. 4(b), the vortices V1 and TV1 generated during the previous upstroke form a vortex loop are connected to V2. They form a vortex loop and moves upward as being convected downstream. The vortex loops generated in sequential flapping periods are connected to form a V-shaped chains with a certain vertical separation, as shown in Fig. 3(b). The wake structures for the fixed wingspan with $AR = 2$ are similar to those with $AR = 4$. However, their sizes for $AR = 2$ are smaller than those for $AR = 4$, seeing Figs. 3(c), 4(c) and 5(c).

The pattern and evolution of wake structures in present paper are consistent with those reported in the previous studies [32-35, 53, 54], although different wing planforms and flapping kinematics are used. The consistency confirms the present results and implies that the wake patterns of a flapping wing are relatively robust.

In Fig. 6, the leading-edge vortex, V3, does not directly connect to tip vortices to form a vortex loop. The vortex V3 sheds from the wing during the transition from downstroke to upstroke, and convects downstream along the upper surface of the wing. Subsequently, it merges with the trailing-edge vortex in the next upstroke. This is different from the vortex V3 in Fig. 5(b) for the fixed wingspan with $AR = 4$, which is fairly uniform along the wingspan, except that the induced velocity of tip vortices tends to push the vortex toward the wing surface near the wingtip. The uniform portion of the vortex V3 is relatively short in the fixed wingspan with $AR = 2$ and the vortex becomes smaller Λ-like, since the tip vortices have a stronger effect at lower aspect ratio. The residence of the separated leading-edge vortex is also reported in the work of Blondeaux et al. [32] and Visbal et al. [55], although the flapping wing geometry and kinematics are different. Visbal et al. [55] did not report the merging of the shed leading-edge vortex with the trailing-edge vortex. It is reasonable inferred that the small angle of attack in the upstroke generates a weak trailing-edge vortex because of the

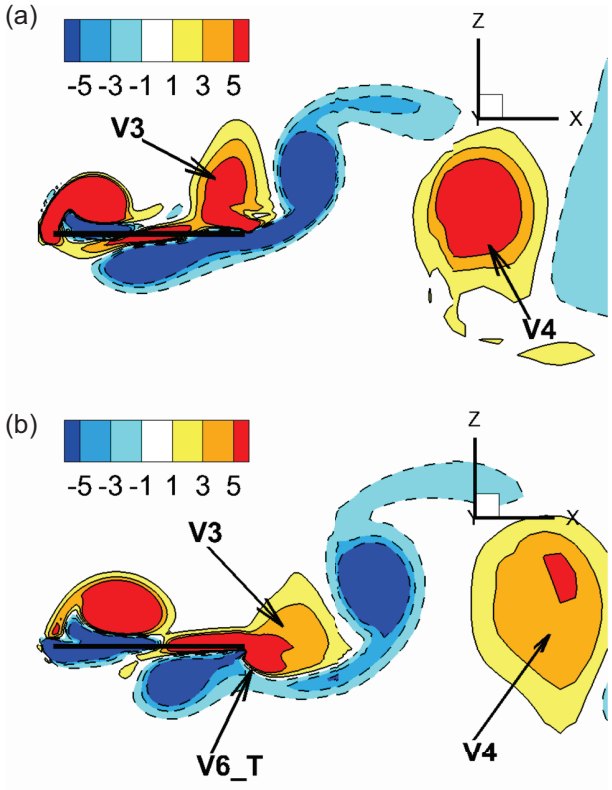

Figure 6 Flow structures in a spanwise slice crossing the flapping wing center for the fixed wingspan case with $AR = 4$. The contours show the value of spanwise vorticity in the slice, (a) at the end of downstroke, (b) in the middle of upstroke. The label V6_T indicates the part of vortex V6 contributed by the trailing-edge vortex, where the vortex V6 is the combination of V3 and the trailing-edge vortex.

non-zero pitch-bias angle in the work of Visbal et al. [55]. The merging of the shedding leading-edge vortex with the trailing-edge vortex is reported in the work of Blondeaux et al. [32], where the flapping wing has a zero pitch-bias angle, and indicates that no new vortex loops appear in the wake. As will be shown in the next subsection, this merging process leads to the unchanged topology of the wake structures although the morphing wingspan changes the evolution of leading-edge vortex.

3.2 Wake pattern of the flapping rectangular wing with morphing wingspan

The wake structures behind the flapping wing with morphing wingspan share some characteristics with those behind the fixed wingspan, such as two vortex loops with opposite signs in each flapping period and forming two oblique chains of interconnected vortex loops. The differences are that the morphing wingspan generates a much larger and stronger vortex loops in downstroke than those in upstroke. As a result, the two branches of the oblique vortex chains are asymmetric, while the lower branch is much wider and stronger than the upper branch, as shown in Fig. 3(a). It is easy to understand that the smaller diameters of the vortex loops result from the smaller wingspan in the upstroke. However, the effects of morphing wingspan are not limited to changing the diameter of the vortex loop. The non-linear interactions between the wing and vortices play an important role. This subsection is devoted to discussing two main vortex dynamics for the evolution of vortex structures.

3.2.1 Shrinking of leading-edge vortex on lower surfaces in downstroke

Figure 4(a) shows the flow structures around the wing at the instant when the wing reaches the end of the downstroke. The leading-edge vortex V3 and the tip vortices TV2 are generated in the downstroke. Because of wingspan retracting, TV2 and part of V3 start to shed from the wing after the middle of the downstroke and are connected to each other. The connection of V3 to TV2 can be seen more clearly in Fig. 5(a), where the wing reaches the middle of upstroke. The vortices V3, TV2 and V2 form a vortex loop in the downstroke. This vortex loop is then cut off by the stretching wingspan after the end of upstroke, as shown in Fig. 7. In the following downstroke, V3 remains on the upper surface of the wing until it merges with the trailing-edge vortex generated in the next upstroke. The geometry and evolution of V3 are similar to those for the fixed wingspan. However, TV2, together with part of V3 cut by the wing, attaches to the lower surface of the wing. The attachment of TV2 to the lower surface of the

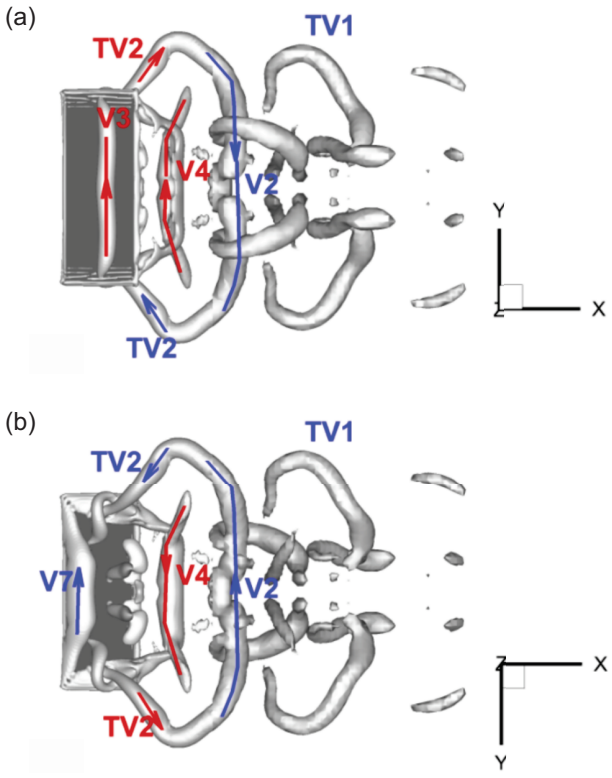

Figure 7 Flow structures around the wing at the end of upstroke, (a) top view, (b) bottom view. The iso-surfaces of $\lambda_2 = -4$ are shown.

wing is significantly different from that for the fixed wing. The TV2, part of V3 cut by the wing, and the newly generated tip vortices form a complex vortex system under the lower surface of the wing (as shown in Figure 7(b)). The non-uniform velocity induced by this complex system destroys the column structure of leading-edge vortex V7, resulting in a weaker V7 on the lower surface of the wing during downstroke, as shown in Fig. 8(a). As discussed in the last subsection, the shedding leading-edge vortex merges with the trailing-edge vortex. Both the V3 and V7 do not independently form vortex structures in the wake. Thus, the morphing wingspan has little effect on the wake topology, although it significantly affects the evolution of leading-edge vortex near the wing surface. Instead of changing wake topology, the shrinking leading-edge vortex, V7, weakens the merging effect and causes a weaker vortex ring in the upstroke. The leading-edge vortex V7 under the lower surface of the wing contributes to a negative lift. The weaker V7 indicates a weaker negative lift. The effect of shrinking leading-edge vortex on the lift coefficient is confirmed in Sect. 4.

3.2.2 Destructive interaction of tip vortices in upstroke

The morphing wingspan also decreases the circulation of the vortex loop by the destructive interactions of the tip vortices. The interactions between tip vortices can be seen from the

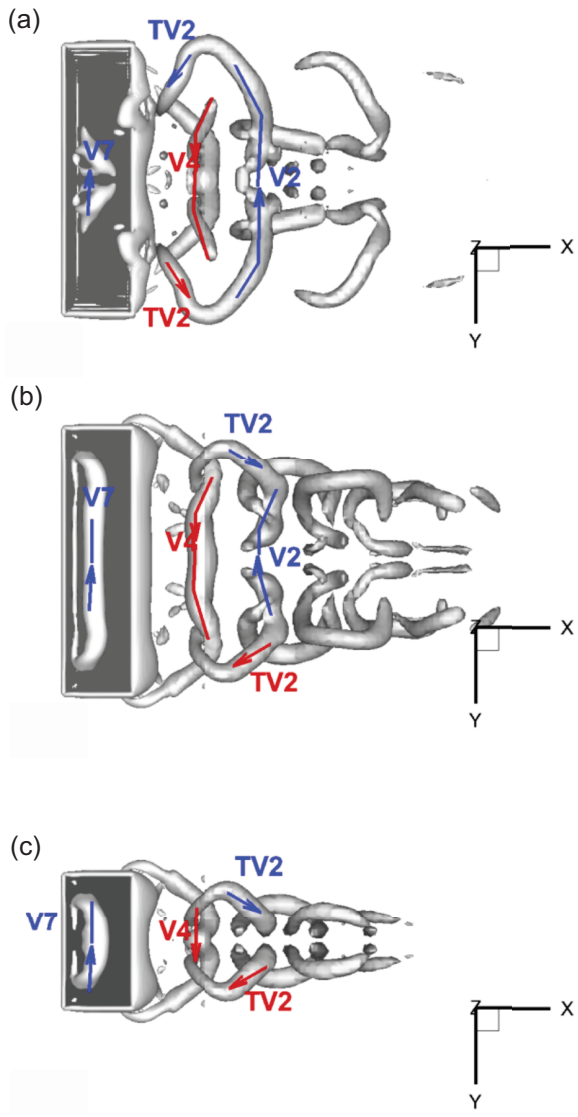

Figure 8 Flow structures around the flapping rectangular wing at the middle downstroke, bottom view, (a) the morphing wingspan case, (b) the fixed wingspan case with $AR = 4$, (c) the fixed wingspan case withy $AR = 2$. The iso-surfaces of $\lambda_2 = -4$ is shown.

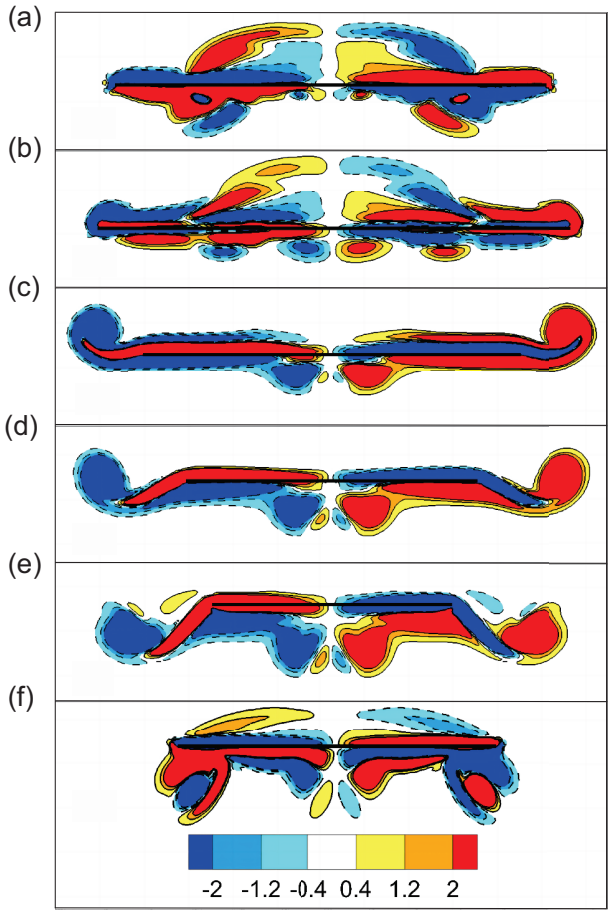

Figure 9 Contours of streamwise vorticity at the slice location of $x = 0.25$. (a) $T^* = 4.11$, about $T/10$ after the start of downstroke; (b) $T^* = 4.23$, near the middle of downstroke; (c) $T^* = 4.47$, near the end of downstroke; (d) $T^* = 4.59$, about $T/10$ after the start of upstroke; (e) $T^* = 4.71$, near the middle of upstroke; (f) $T^* = 4.95$ near the end of upstroke.

streamwise vorticity contours at the slice location of $x = 0.25$ (3/4 chord from the leading edge) in Fig. 9, where a weaker tip vortex is generated during the upstroke. The weaker tip vortices generated during upstroke are as follows. The tip vortices generated during the downstroke are able to convect to the lower surface of the plate as the wingspan becomes smaller during upstroke. The tip vortices generated during downstroke carry the opposite sign to that of the tip vortices generated during upstroke. Through their interactions, part of the opposite-sign vorticity of the downstroke tip vortices is involved into the upstroke tip vortices, resulting in weakened upstroke tip vortices. According to the Kelvin-Helmholtz vorticity conservation theorem, the weaker tip vortices cause a decrement in circulation when they connect to the trailing-edge vortices to form a weaker uprising vortex loop than the downward vortex loop. Therefore, this destructive interaction of tip vortices is another vortex dynamics mechanism caused by the morphing wingspan to change the vortex structures.

From the point of view of vorticity impulse, the asymmetry of the tip vortices during downstroke and upstroke, as shown in Fig. 9, clearly results in a net downward impulse. This is because the z-direction impulse in the Trefftz plane can be calculated as the integration of the first y-moment of x-vorticity [56]:

$$I_z = \int_{\Omega} y\omega_x \mathrm{d}\Omega, \tag{6}$$

where Ω is the area of the Trefftz plane in the wake. During downstroke, the stronger tip vortices lead to higher ω_x and, along with the wider-spread tip vortices due to wingspan stretching, resulting in a larger downward impulse. This is also evident in the larger, stronger downward branch of the wake in comparison to the smaller, weaker upward branch of

the wake shown in Fig. 3(a). The downward asymmetry of the wake provides the same reason that there is a net upward force on the flapping wing exerted by the flow.

4. Lift coefficient

4.1 Lift enhancement by the morphing wingspan

Aerodynamic forces are used to investigate the lift enhancement by morphing wingspan, which are dependent on vortex intensity. The lift coefficient is defined as

$$C_l(t) = \frac{F_z(t)}{0.5\rho U_\infty^2 S(t)}, \tag{7}$$

where $F_z(t)$ is the vertical component of the instantaneous aerodynamic force, and $S(t)$ is the instantaneous planform area of the wing. Based on the definition of Eq. (7), the non-circulation added mass effect contributes the same portion to the lift coefficient in all the cases of this work, since the same heaving kinematics is used. Figure 10 shows the time history of lift coefficient in one single period.

In the case of the fixed wingspan ($SR = 1.0$), the lift coefficients are symmetric which is consistent with the symmetric vortex distribution in the wake. In the case of the morphing wingspan, the positive lift coefficients generated in downstroke are larger than the negative lift coefficients generated in upstroke, which is consistent with the asymmetric vortex distributions in the wake. The time-averaged lift coefficient is 0.42, which is the net lift coefficient generated by the morphing wingspan effect. This amount of the lift increase is significant. For instance, in the study by Taira and Colonius [57], the maximum time-averaged lift coefficient of a stationary rectangular wing with a fixed aspect ratio of 4 is 0.8, achieved near a post-stall angle of attack of 30° at the same Reynolds number of 300. It is noted that the angle of attack for the steady wings in the present study is zero.

The asymmetric of the lift coefficient or wake structures results from the morphing wingspan. The effect of morphing wingspan is two-fold: (1) the influence of aspect ratio; (2) spanwise flow motion and wingtip position due to spanwise motion of the plate. Their effects on the lift coefficient and wake structures are discussed in the following subsections.

4.2 Effect of aspect ratio

According to the classical aerodynamics [58] for a fixed rectangular wing in steady flow, the lift coefficient of the wing with the same cross section can be given in the form of $Cl = \beta Cl_0$. Here Cl_0 is the lift coefficient of the wing with an infinite wingspan and β is a factor related to aspect ratio. In case of morphing wings, the lift coefficient increases with the wingspan, since the large distance between the tip vortices causes a weak negative induced angle of attack due to decreased downwash.

The present work for the flapping flat-plate rectangular wing shows that the changes of lift coefficients have the same trend as those for a stationary wing when the aspect ratio changes. This can be seen from Fig. 11 in which the peak lift coefficient monotonously increases with the aspect ratio. Since the time-averaged aspect-ratio in downstroke is larger than that in upstroke in the morphing wingspan, there will be

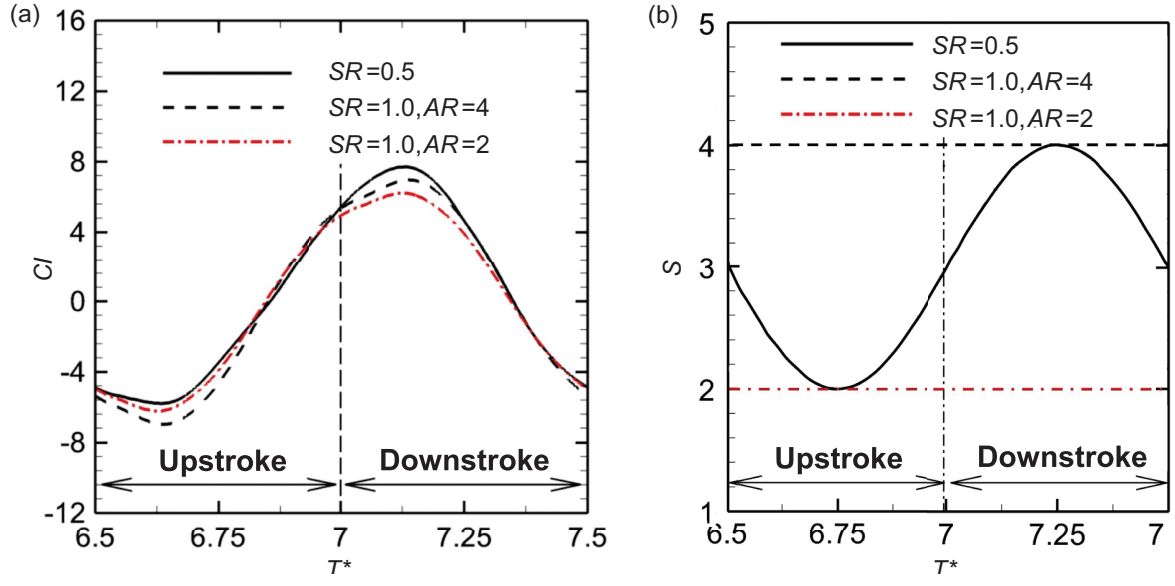

Figure 10 Comparisons of (a) lift coefficients and (b) wing area for the morphing wingspan case and fixed wingspan cases.

positive lift generated in one flapping cycle. However, Fig. 10 indicates that the positive peak of the lift coefficient of the morphing wingspan is larger than that of the fixed wingspan case with $AR = 4$ and the magnitude of the negative peak of the lift coefficient of the morphing wingspan is smaller than that of the fixed wingspan case with $AR = 2$. Therefore, the morphing wingspans exhibit the dynamic effect in additional to the geometrical effect.

The present work for the flapping flat-plate rectangular wing shows that the changes of lift coefficients have the same trend as those for a stationary wing when the aspect ratio changes. This can be seen from Fig. 11 in which the peak lift coefficient monotonously increases with the aspect ratio. Since the time-averaged aspect-ratio in downstroke is larger than that in upstroke in the morphing wingspan, there will be positive lift generated in one flapping cycle. However, Fig. 10 indicates that the positive peak of the lift coefficient of the morphing wingspan is larger than that of the fixed wingspan case with $AR = 4$ and the magnitude of the negative peak of the lift coefficient of the morphing wingspan is smaller than that of the fixed wingspan case with $AR = 2$. Therefore, the morphing wingspans exhibit the dynamic effect in additional to the geometrical effect.

4.3 Effect of slip boundary conditions on lift coefficients

We consider the fixed wingspan ($SR = 1$) with the following slip velocity on wing surface, which represents the fluid motion associated with the spanwise morphing:

$$V_w = -2\pi f b L_0 s \cdot \cos(2\pi f t + \varphi), \tag{8}$$

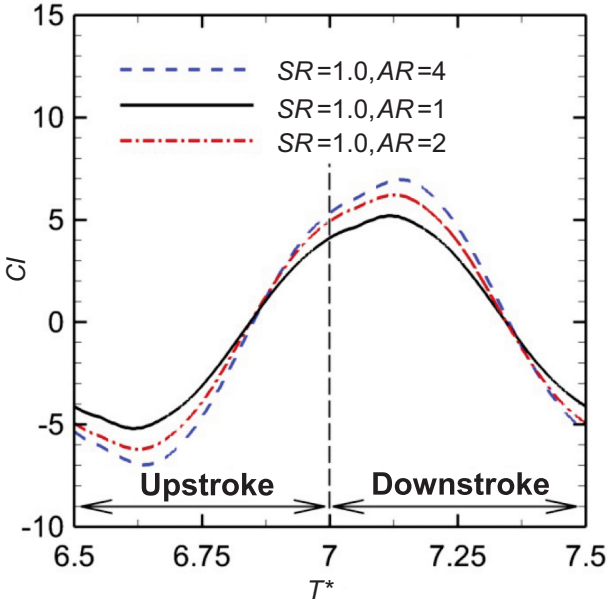

Figure 11 Instantaneous lift coefficient histories of a heaving flat plate with $AR = 1.0$, 2.0, and 4.0.

where $s = y_0/(0.5L_0)$ and y_0 is the initial spanwise coordinate of each point on the wing. Therefore, Eq. (8) represents a linear velocity profile in the spanwise directions and gives the boundary condition for the flows on wing surface. The lift coefficients obtained are compared with those of the fixed wingspan ($SR = 1$) and the morphing wingspan ($SR = 0.5$), where the non-slip velocity boundary conditions are imposed on the wing surfaces. Figure 12 plots the lift coefficients for the above three cases with $AR = 4$. It is observed that there are no much differences between the slip and non-slip boundary conditions. It may imply that spanwise flows have little effects on the list coefficients.

We change the slip velocity on wing surface as $V_w = 0$ to better understand its effects on lift coefficients. Figure 13 compares the three lift coefficients for the morphing wing ($SR = 0.5$) and the fixed wingspans ($SR = 1.0$) with the slip and nonslip velocity boundary conditions. Obviously, the three lift curves are very closed to each other, which is consistent with the observation in Fig. 12.

4.4 Effect of the non-symmetric span length changes

This subsection is devoted to isolating the effect of changing the position of the tips to investigate the effects of the non-symmetric wingspan changes. For this purpose, the spanwise velocity is forced to zero on the surface of the wing, i.e., $V_w = 0$, instead of the velocity that moves with the wingspan morphing motion. Therefore, the wingspan changes the size, but the fluid on the wing surface does not move along the wingspan. Figure 13 shows that the lift coefficients in this case are almost the same as those in the case of morphing wingspan. The morphing wingspans generate not only the geometrical effect discussed in Sect. 4.2, but also the vortex dynamic effects. The vortex loops are cut to cause shrinkage of the leading-edge vortex under the wing and thus destructive interactions of wing-tip vortices during upstroke. The obtained result is also consistent with the discussion in Sect. 4.3, where the spanwise flows associated to the spanwise velocity of the wing are shown to have little effect on the lift coefficients and flow structures.

5. Conclusions

The effects of morphing wingspan on the wake structures are not well understood, although the morphing wingspan widely exists in biolocomotions. This work employs a bio-inspired flapping wing model to investigate the effect of morphing wingspan on wake structures. The model consists of a rectangular flat-plate wing heaving harmonically in a uniform incoming flow. The wingspan changes during heaving, with a

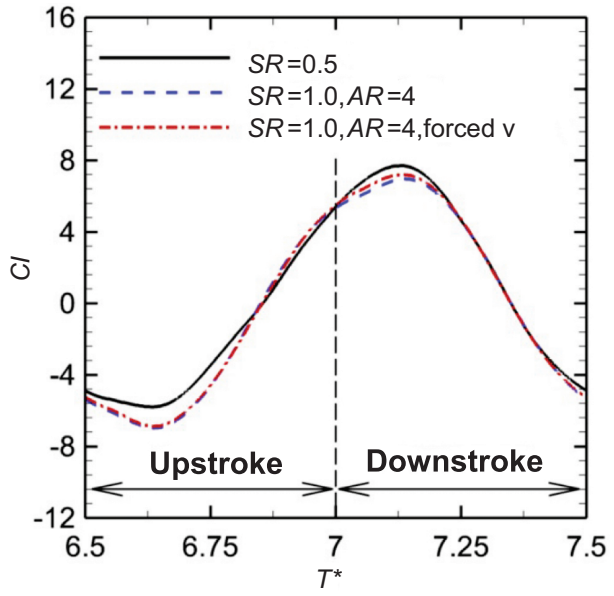

Figure 12 Comparisons of lift coefficient for the morphing wingspan case, the fixed wingspan cases with $AR = 4$. The forced v in the label represents the modified fixed wingspan case with forced spanwise velocity

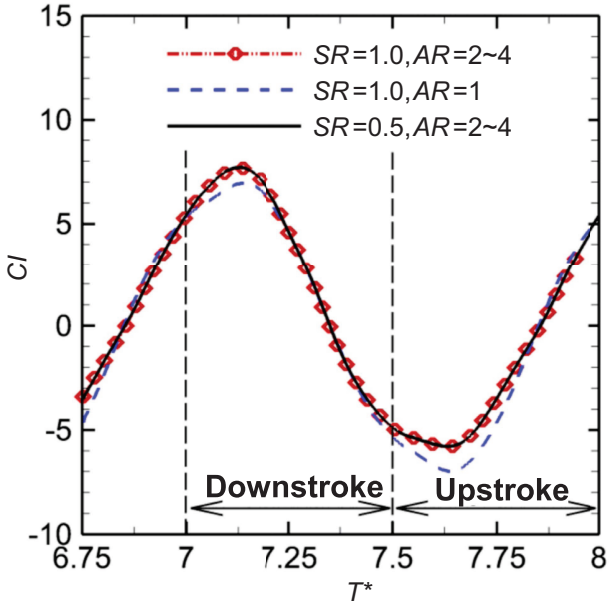

Figure 13 Histories of the lift coefficient of morphing wingspan cases and fixed wingspan case. The lable $SR = 0.5, AR = 2 \sim 4$ represents the morphing wingspan case. The label $AR = 1.0, AR = 2 \sim 4$ represents the modified morphing wingspan case.

maximum wingspan at the middle of downstroke and minimum wingspan at the middle of upstroke. The Reynolds number based on the velocity magnitude of the incoming flow and chord length is 300. The wake structures of the typical morphing wingspan case at the Strouhal number (based on the flapping frequency and tip-to-tip flapping amplitude) of 0.3 and span ratio (the ratio between the minimum wingspan and maximum wingspan) of 0.5 are studied in detail by comparing with the corresponding fixed wingspan cases. The results show that the morphing wingspan does not change the topology of the wake structures, but significantly affects the circulation and evolution of the vortices near the wing surface.

The wake structures of all the morphing and fixed wingspan cases in this work can be described by the same wake model: two oblique chains of interconnected vortex loops, convecting downstream in the "V" shape with a separation in the vertical direction. The difference is that the morphing wingspan case has an asymmetric distribution of the vortex chains in the wake, with the lower branch of the vortex loop much wider and stronger than the upper branch. The asymmetric distribution of vortex chains results from both the geometrical effect and the vortex interactions. The vortex interactions are identified as: (1) the shrinking of the leading-edge vortex under the lower surface of the wing in downstroke; (2) the destructive interactions of tip vortices during upstroke. The analysis on the lift coefficients shows that the above vortex interactions are mainly caused by the asymmetric change of the wingspan in the downstroke and upstroke. The spanwise flow associated to the spanwise morphing contributes little to the asymmetric distribution of vortex chains.

This work indicates morphing wingspan can generate complex flow structures near the flapping wing surface. But the change of wake topology reported in the bat flight may not be solely contributed by the morphing wingspan. The change of the wake topology may be related to the other particular kinematics in bat flight, such as bias-pitching, flexion between outer wing and inner wing, or their combined effect with morphing wingspan, which is a topic for future work.

Author contributions ***Xinyi He:*** *Writing – original draft, Investigation, Validation.* ***Yi Liu:*** *Formal analysis, Software.* ***Yixin Chen:*** *Visualization, Data curation.* ***Shizhao Wang:*** *Conceptualization, Writing – review & editing, Supervision, Funding acquisition.*

Acknowledgements *This work was supported by Basic Science Center Program of the National Natural Science Foundation of China for "Multiscale Problems in Nonlinear Mechanics" (Grant No. 11988102), the National Natural Science Foundation of China (Grant Nos. 12102439, 92252203, and 91952301), and the China Postdoctoral Science Foundation (Grant No. 2021M703290). The computations were conducted on Tianhe-3F at the National Supercomputer Center in Tianjin.*

1 G. R. Spedding, and A. Hedenström, PIV-based investigations of animal flight, Exp. Fluids **46**, 749 (2009).
2 J. O. Dabiri, Optimal vortex formation as a unifying principle in biological propulsion, Annu. Rev. Fluid Mech. **41**, 17 (2009).
3 J. D. Zhang, Q. H. Zuo, M. D. Lin, W. X. Huang, W. J. Pan, and G. X. Cui, Evolution of vortices in the wake of an ARJ21 airplane: Application of the lift-drag model, Theor. Appl. Mech. Lett. **10**, 419 (2020).
4 X. Meng, and M. Sun, Wing kinematics, aerodynamic forces and vortex-wake structures in fruit-flies in forward flight, J. Bionic Eng.

13, 478 (2016).
5 Y. Wang, X. He, G. He, Q. Wang, L. Chen, and X. Liu, Aerodynamic performance of the flexibility of corrugated dragonfly wings in flapping flight, Acta Mech. Sin. **38**, 322038 (2022).
6 D. Zhang, J. D. Zhang, and W. X. Huang, Physical models and vortex dynamics of swimming and flying: A review, Acta Mech. **233**, 1249 (2022).
7 X. T. Huang, P. N. Sun, H. G. Lyu, and S. Y. Zhong, Study of 3D self-propulsive fish swimming using the δ^+-SPH model, Acta Mech. Sin. **39**, 722053 (2023).
8 G. He, G. Jin, and Y. Yang, Space-time correlations and dynamic coupling in turbulent flows, Annu. Rev. Fluid Mech. **49**, 51 (2017).
9 Z. Jane Wang, Two dimensional mechanism for insect hovering, Phys. Rev. Lett. **85**, 2216 (2000).
10 M. A. Ashraf, J. Young, and J. C. S. Lai, Reynolds number, thickness and camber effects on flapping airfoil propulsion, J. Fluids Struct. **27**, 145 (2011).
11 D. Majumdar, S. Ravi, and S. Sarkar, Passive dynamics regulates aperiodic transitions in flapping wing systems, PNAS Nexus, 2023, doi: 10.1093/pnasnexus/pgad086.
12 Y. Xiang, H. Hang, S. Qin, and H. Liu, Scaling analysis of the circulation growth of leading-edge vortex in flapping flight, Acta Mech. Sin. **37**, 1530 (2021).
13 M. Zhang, Q. Wu, B. Huang, and G. Wang, Lagrangian-based numerical investigation of aerodynamic performance of an oscillating foil, Acta Mech. Sin. **34**, 839 (2018).
14 J. M. Anderson, K. Streitlien, D. S. Barrett, and M. S. Triantafyllou, Oscillating foils of high propulsive efficiency, J. Fluid Mech. **360**, 41 (1998).
15 X. Lin, J. Wu, and T. Zhang, Performance investigation of a self-propelled foil with combined oscillating motion in stationary fluid, Ocean Eng. **175**, 33 (2019).
16 G. Y. Dynnikova, Y. A. Dynnikov, S. V. Guvernyuk, and T. V. Malakhova, Stability of a reverse Karman vortex street, Phys. Fluids **33**, 024102 (2021).
17 B. Turhan, Z. Wang, and I. Gursul, Interaction of vortex streets with a downstream wing, Phys. Rev. Fluids **7**, 094701 (2022).
18 L. Schouveiler, F. S. Hover, and M. S. Triantafyllou, Performance of flapping foil propulsion, J. Fluids Struct. **20**, 949 (2005).
19 L. Tian, Z. Zhao, W. Wang, and N. Liu, Length and stiffness effects of the attached flexible plate on the flow over a traveling wavy foil, Acta Mech. Sin. **37**, 1404 (2021).
20 Y. W. Jung, and S. O. Park, Vortex-shedding characteristics in the wake of an oscillating airfoil at low Reynolds number, J. Fluids Struct. **20**, 451 (2005).
21 X. Lin, J. Wu, T. Zhang, and L. Yang, Phase difference effect on collective locomotion of two tandem autopropelled flapping foils, Phys. Rev. Fluids **4**, 054101 (2019).
22 X. Lin, G. He, X. He, and Q. Wang, Dynamic response of a semi-free flexible filament in the wake of a flapping foil, J. Fluids Struct. **83**, 40 (2018).
23 Z. C. Zheng, and Z. Wei, Study of mechanisms and factors that influence the formation of vortical wake of a heaving airfoil, Phys. Fluids **24**, 103601 (2012).
24 Z. Wei, and Z. C. Zheng, Mechanisms of wake deflection angle change behind a heaving airfoil, J. Fluids Struct. **48**, 1 (2014).
25 B. Li, X. Zhang, and X. Zhang, Classifying wakes produced by self-propelled fish-like swimmers using neural networks, Theor. Appl. Mech. Lett. **10**, 149 (2020).
26 I. Fenercioglu, and O. Cetiner, Categorization of flow structures around a pitching and plunging airfoil, J. Fluids Struct. **31**, 92 (2012).
27 G. R. Abdizadeh, M. Farokhinejad, and S. Ghasemloo, Numerical investigation on the aerodynamic efficiency of bio-inspired corrugated and cambered airfoils in ground effect, Sci. Rep. **12**, 19117 (2022).
28 L. Liu, G. He, X. He, Q. Wang, and L. Chen, Numerical study on the effects of a semi-free and non-uniform flexible filament in different vortex streets, Acta Mech. Sin. **37**, 929 (2021).
29 X. Zhu, G. He, and X. Zhang, How flexibility affects the wake symmetry properties of a self-propelled plunging foil, J. Fluid Mech. **751**, 164 (2014).
30 C. Koehler, P. Beran, M. Vanella, and E. Balaras, Flows produced by the combined oscillatory rotation and translation of a circular cylinder in a quiescent fluid, J. Fluid Mech. **764**, 148 (2015).
31 K. D. von Ellenrieder, K. Parker, and J. Soria, Flow structures behind a heaving and pitching finite-span wing, J. Fluid Mech. **490**, 129 (2003).
32 P. Blondeaux, F. Fornarelli, L. Guglielmini, M. S. Triantafyllou, and R. Verzicco, Numerical experiments on flapping foils mimicking fish-like locomotion, Phys. Fluids **17**, 113601 (2005).
33 H. Dong, R. Mittal, and F. M. Najjar, Wake topology and hydrodynamic performance of low-aspect-ratio flapping foils, J. Fluid Mech. **566**, 309 (2006).
34 J. H. J. Buchholz, and A. J. Smits, On the evolution of the wake structure produced by a low-aspect-ratio pitching panel, J. Fluid Mech. **546**, 433 (2006).
35 J. H. J. Buchholz, and A. J. Smits, The wake structure and thrust performance of a rigid low-aspect-ratio pitching panel, J. Fluid Mech. **603**, 331 (2008).
36 T. O. Yilmaz, and D. Rockwell, Three-dimensional flow structure on a maneuvering wing, Exp. Fluids **48**, 539 (2010).
37 M. A. Green, C. W. Rowley, and A. J. Smits, The unsteady three-dimensional wake produced by a trapezoidal pitching panel, J. Fluid Mech. **685**, 117 (2011).
38 O. Barannyk, B. J. Buckham, and P. Oshkai, On performance of an oscillating plate underwater propulsion system with variable chordwise flexibility at different depths of submergence, J. Fluids Struct. **28**, 152 (2012).
39 H. Dai, H. Luo, P. J. S. A. F. de Sousa, and J. F. Doyle, Thrust performance of a flexible low-aspect-ratio pitching plate, Phys. Fluids **24**, 101903 (2012).
40 L. Yan, J. Pan, and C. Shao, Modes of vortex shedding from a rotary oscillating plate, Acta Mech. Sin. **38**, 321481 (2022).
41 T. Liu, S. Jones, K. Kuykendoll, and R. Rhew, Avian wing geometry and kinematics, AIAA J. **44**, 954 (2006).
42 J. A. Cheney, J. P. J. Stevenson, N. E. Durston, M. Maeda, J. Song, D. A. Megson-Smith, S. P. Windsor, J. R. Usherwood, and R. J. Bomphrey, Raptor wing morphing with flight speed, J. R. Soc. Interface. **18**, 20210349 (2021).
43 C. Harvey, V. B. Baliga, J. C. M. Wong, D. L. Altshuler, and D. J. Inman, Birds can transition between stable and unstable states via wing morphing, Nature **603**, 648 (2022).
44 C. Harvey, L. L. Gamble, C. R. Bolander, D. F. Hunsaker, J. J. Joo, and D. J. Inman, A review of avian-inspired morphing for UAV flight control, Prog. Aerosp. Sci. **132**, 100825 (2022).
45 M. Wolf, L. C. Johansson, R. von Busse, Y. Winter, and A. Hedenström, Kinematics of flight and the relationship to the vortex wake of a Pallas' long tongued bat (Glossophaga soricina), J. Exp. Biol. **213**, 2142 (2010).
46 A. Hedenström, L. C. Johansson, M. Wolf, R. von Busse, Y. Winter, and G. R. Spedding, Bat flight generates complex aerodynamic tracks, Science **316**, 894 (2007).
47 S. Wang, X. Zhang, G. He, and T. Liu, Lift enhancement by dynamically changing wingspan in forward flapping flight, Phys. Fluids **26**, 061903 (2014), arXiv: 1309.2726.
48 S. Wang, and X. Zhang, An immersed boundary method based on discrete stream function formulation for two- and three-dimensional incompressible flows, J. Comput. Phys. **230**, 3479 (2011).
49 X. Yang, X. Zhang, Z. Li, and G. W. He, A smoothing technique for discrete delta functions with application to immersed boundary method in moving boundary simulations, J. Comput. Phys. **228**, 7821 (2009).
50 S. Wang, G. He, and X. Zhang, Parallel computing strategy for a flow solver based on immersed boundary method and discrete stream-function formulation, Comput. Fluids **88**, 210 (2013).
51 S. Wang, X. Zhang, G. He, and T. Liu, A lift formula applied to low-

Reynolds-number unsteady flows, Phys. Fluids **25**, 093605 (2013).
52 J. Jeong, and F. Hussain, On the identification of a vortex, J. Fluid. Mech. **285**, 69 (1995).
53 A. K. De, and S. Sarkar, Spatial wake transition past a thin pitching plate, Phys. Rev. E **104**, 025106 (2021).
54 A. K. De, and S. Sarkar, Dependence of wake structure on pitching frequency behind a thin panel at *Re* = 1000, J. Fluid Mech. **924**, A33 (2021).
55 M. Visbal, T. O. Yilmaz, and D. Rockwell, Three-dimensional vortex formation on a heaving low-aspect-ratio wing: Computations and experiments, J. Fluids Struct. **38**, 58 (2013).
56 Z. C. Zheng, Betz invariants and generalization of vorticity moment invariants, AIAA J. **39**, 431 (2001).
57 K. Taira, and T. Colonius, Three-dimensional flows around low-aspect-ratio flat-plate wings at low Reynolds numbers, J. Fluid Mech. **623**, 187 (2009).
58 J. Anderson, and J. D. Anderson, Fundamentals of Aerodynamics, 5 ed. (McGraw-Hill, Columbus, 2010).

变翼展的仿生扑翼尾迹特征

何心怡, 刘毅, 陈一鑫, 王士召

摘要 本文基于仿生扑翼流动的数值模拟研究变形翼展对尾迹结构的影响. 所采用的扑翼模型为一个在均匀来流中上下扑动的平板. 翼展随着扑动而变化, 最大翼展在下扑行程的中间, 最小翼展在上挥行程的中间. 其尾迹的特征表现为两条相互连接的倾斜涡链. 虽然变形翼展对尾流拓扑结构的影响不大, 但它显著影响了扑翼附近涡结构, 导致尾流中涡环链的分布不对称. 下扑过程中, 位于扑翼下表面的前缘涡收缩, 与上挥中翼尖涡相互作用, 通过分析升力系数, 发现上述涡的相互作用是由翼展长度的变化引起的.